Available online at www.sciencedirect.com

ScienceDirect

journal homepage: www.elsevier.com/locate/he

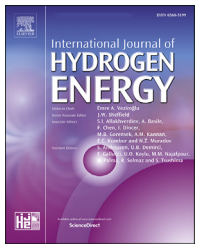

Achieving the dehydriding reversibility and elevating the equilibrium pressure of YFe_2 alloy by partial Y substitution with Zr

Haoliang Pang [a], *Ziming Li* [a], *Chao Zhou* [a], *Hui Wang* [a], *Liuzhang Ouyang* [a,c], *Shurong Yuan* [b], *Yujun Zhao* [b], *Min Zhu* [a,*]

[a] *School of Materials Science and Engineering and Guangdong Provincial Key Laboratory of Advanced Energy Storage Materials, South China University of Technology, Guangzhou, 510641, China*

[b] *Department of Physics, South China University of Technology, Guangzhou 510640, China*

[c] *China-Australia Joint Laboratory for Energy & Environmental Materials, South China University of Technology, Guangzhou, 510641, China*

ARTICLE INFO

Article history:
Received 9 February 2018
Received in revised form
1 April 2018
Accepted 31 May 2018
Available online 29 June 2018

Keywords:
Hydrogen storage alloys
YFe_2
Zr substitution
Hydrogenation thermodynamics

ABSTRACT

To overcome the hydrogen-induced amorphization and phase disproportionation in the fast de-/hydrogenation of YFe_2, the alloying of partial substituting Y with Zr was carried out to obtain $Y_{1-x}Zr_xFe_2$ ($x = 0.1, 0.2, 0.3, 0.5$) alloys. All Y–Zr–Fe alloys remained single C15 Laves phase structure at states of as-annealed, hydrogenated and dehydrogenated. With the increasing of Zr content, the Y–Zr–Fe alloys showed the decrease in the lattice constants and hydrogenation capacity, but the increase in the dehydrogenation capacity and dehydriding equilibrium pressure. The alloy $Y_{0.9}Zr_{0.1}Fe_2$ showed maximum initial hydrogenation capacity of 1.87 wt% H, while the alloy $Y_{0.5}Zr_{0.5}Fe_2$ showed highest desorption capacity of 1.26 wt% with obvious dehydriding plateau. Based on experiment analysis and first principle calculation of binding energy, the great improvement in the dehydriding thermodynamics for Y–Zr–Fe alloys is attributed to the change in the unit cell volume, electron concentration and stability of hydrides due to the Zr substitution.

Introduction

The interaction of hydrogen with intermetallic compounds has been widely investigated because of their applications in solid-state hydrogen storage, hydrogen separation, hydrogen purification and hydrogen sensor [1–4]. Those intermetallic compounds generally consist of strong hydride-forming elements A and weak hydride-forming elements B to obtain adequate formation enthalpy (20–40 kJ/mol H_2) of hydrides [5]. Various A_xB_y intermetallic compounds with different crystal structures have been developed as interstitial hydrogen storage alloys. The AB_2 intermetallics with different Laves phase structures, is one type of important hydrogen storage alloy with the A-elements of Ti, Zr, Y etc. and the B-elements of V, Cr, Mn, Fe.

Many different AB_2 type alloys have been developed so far for hydrogen storage and some of them have been successfully used in important applications. For instance, the AB_2

* *Corresponding author.*
E-mail address: memzhu@scut.edu.cn (M. Zhu).

https://doi.org/10.1016/j.ijhydene.2018.05.161

type Zr–Ti–V–Cr alloy is used as negative electrode in Ni-MH battery with much higher capacity than that of AB_5 alloys [6–8], while the AB_2 type Ti–Cr–Mn alloy has been applied in hybrid hydrogen tank [9]. In addition, the $ZrFe_2$ alloy with C15 structure shows the high-pressure hydrogen storage characteristic [10,11], and thus it also has potential application for hybrid high pressure metal hydride tank [12].

The other type of AB_2 alloys with the A-side of rare earth elements (Y, La, *etc.*) and B-side transition metals (Fe, Ni, Co, *etc.*) have C14 or C15 Laves phase structure. However, most of them are not suitable for hydrogen storage application, because hydrogen-induced amorphization (HIA) and disproportionation were unavoidable in the de-/hydrogenation process in this type of AB_2 alloys [8,13–21]. Take the YFe_2 for example, it can absorb deuterium up to 4.2 D/f.u. under moderate temperature and deuterium pressure, and the crystalline deuterides with various structures can be obtained at different deuterium content [22]. However, when the hydrogenation temperature is elevated or fast during the hydrogen absorption of YFe_2, the tendency is to form amorphous hydrides and finally decompose into Y hydride and Fe particles as observed by Aoki and Li et al. [23,24]. Therefore, the challenge of the present work is to absorb and desorb hydrogen with fast kinetic in YFe_2 while avoiding amorphization and disproportionation.

Different viewpoints have been proposed to explain the HIA and disproportionation of this type of AB_2 intermetallics. Some researchers [25–27] attributed the HIA to over large negative mixing heat between H and A-side metal atoms, and a faster mobility of at least one element (*i.e.* hydrogen) than the mobility of metallic constituents, which would inhibit the nucleation and growth of more stable crystalline counterparts. Chung et al. [25] assumed that the elastic softening of a compound occurred before the amorphization, and that the solid-state amorphization was triggered by the elastic instability of a compound. Namely that, the hydrogen absorption results in lattice expansion and elastic stain. As the elastic stress exceeds the elastic limit, the compound cannot preserve its original state any more [28]. For that, some researchers believed that the compounds with higher bulk modulus could prevent the amorphization [29].

Alloying is mostly widely used method to improve the hydrogen storage properties of various alloys, but there is few successful report on the reversible hydrogen storage properties of YFe_2-based alloy. Recently, the reversible hydrogen storage of YFe_2 alloys was achieved by partial Al substitution of Fe [23], and that the C15 structure of Y–Fe–Al alloys could be maintained during the de-/hydrogenation cycle, and no disproportionation and amorphization occurred at de-/hydrogenation states. However, the Y–Fe–Al alloys showed rather low hydrogen desorption equilibrium pressure, and no distinct hydriding and dehydriding plateau could be observed in the pressure-composition isotherms. The low dehydriding equilibrium pressure results in incomplete dehydrogenation at ambient temperature and pressure.

Kojima et al. [30] proposed that the dissociation pressure of hydrogen storage alloys increased with the smaller unit cell volume and higher bulk modulus of constituent elements, because the hydrogenation process would become more difficult due to higher elastic stress imposed by hydrogen atoms, and the hydrides would become more unstable. In addition, Ramesh and Kesavan et al. [31–34] found that the hydrogen desorption plateau pressure of pseudo-binary Zr–Ho–Co system with the C15-type Laves phase structure was raised by partial replacement of Ho by Zr. Therefore, to improve the hydrogen storage thermodynamic properties of YFe_2 alloys, it is feasible to modify the composition and structure of YFe_2 alloy by A-site Zr substitution. On the hand, the atomic radius of Zr (1.59 Å) is smaller than that of Y (1.78 Å). On the other hand, the Zr metal has higher bulk modulus (91 GPa) than that of the Y metal (41.2 GPa). Paul-Boncour et al. [35] found that $ZrFe_2$ can absorb deuterium up to 2.7 D/f.u. under a very high pressure and the deuteride can remain C15 Laves phase structure. Hence, the C15 Laves phase structure could be observed in the hydrides of Y–Zr–Fe system.

In this work, we partially substituted Y of A-site by Zr to improve the reversible hydrogen storage properties. The structure and hydrogen storage properties of Y–Zr–Fe alloys were investigated. In addition, the binding energies of different tetrahedral interstitial sites occupied with hydrogen atoms were calculated by first principle calculations based on the density function theory [36–38], and the calculation results could well explain the change in the thermodynamic stability of the Y–Zr–Fe hydrides with different Zr content.

Experimental details and computational method

Y, Zr, and Fe ingots (all of 99.9% purity) were used as raw materials. The $Y_{1-x}Zr_xFe_2$ ($x = 0.1, 0.2, 0.3, 0.5$) alloys were prepared by arc melting in the water-cooled copper crucible under Ar atmosphere. Before melting, the Y, Zr and Fe bulks were polished by a grinder to remove the oxidation layer. The melted ingots were remelted for six times to ensure compositional homogeneity, and the as-melted ingots were then sealed in evacuated silica tube and annealed at 1100 °C to avoid second phase precipitation. The as-annealed ingots were crushed into powders and sieved by a 200 mesh sieve in the glove box for further measurements.

The phase structure of powder samples was characterized by X-ray diffraction (XRD) with Cu-Kα radiation at 45 kV and 40 mA (PANalytical Empyrean). Rietveld structure refinements were conducted by using the Highscore Plus software. The microstructure and composition of alloys at different states were investigated by scanning electron microscope (SEM, Zeiss Supra 40/VP) equipped with an energy-dispersive spectrometer (EDS). The hydrogen storage properties including the isothermal de-/hydrogenation kinetics and pressure-composition isotherm (PCI) were measured using a Sieverts-type automatic gas reaction controller (Advanced Materials Corporation). The sample of approximate 0.3 g were put into the sample holder and kept under vacuum at 200 °C for 2 h as an activation treatment before the de-/hydrogenation measurement. The isothermal hydrogenation kinetic test was carried out under 4 MPa H_2 at 100 °C, while the dehydrogenation kinetic test was performed at 100 °C, 200 °C and 300 °C. The samples were fully dehydrogenated by vacuuming at 300 °C for 2 h before rehydrogenation test. The desorption PCI curve was measured at a pressure range of 0.002–1.5 MPa at 200 °C.

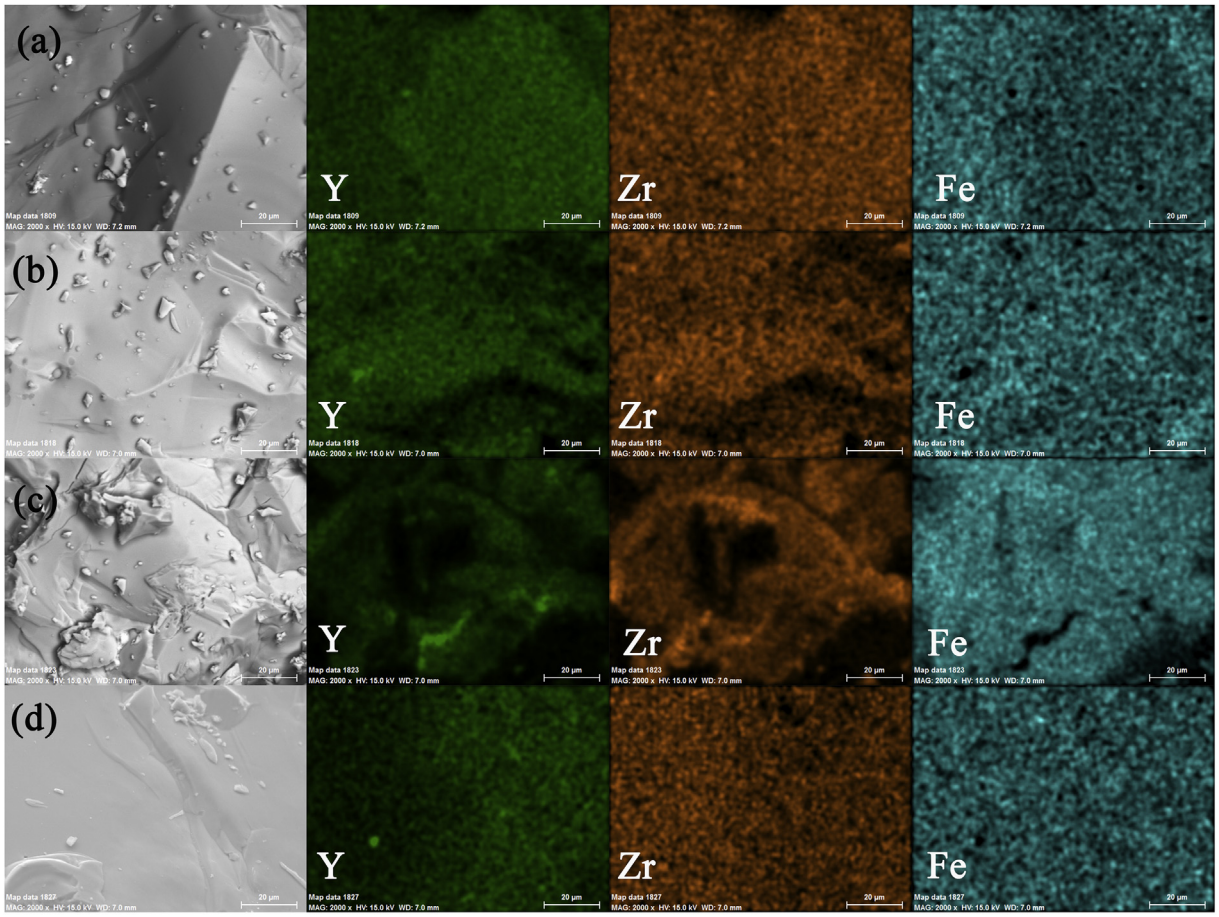

Fig. 1 – SEM back-scattering images and the distribution of Y, Zr and Fe elements of (a) $Y_{0.9}Zr_{0.1}Fe_2$; (b) $Y_{0.8}Zr_{0.2}Fe_2$; (c) $Y_{0.7}Zr_{0.3}Fe_2$; (d) $Y_{0.5}Zr_{0.5}Fe_2$.

Table 1 – The composition of as-annealed Y, Zr and Fe of $Y_{1-x}Zr_xFe_2$ alloys.

Alloys	Atomic percentage/at. % (±0.1%)			Y: Zr: Fe
	Y	Zr	Fe	
$Y_{0.9}Zr_{0.1}Fe_2$	29.8	3.2	67.0	0.89:0.10:2.00
$Y_{0.8}Zr_{0.2}Fe_2$	26.7	6.8	66.5	0.80:0.20:2.00
$Y_{0.7}Zr_{0.3}Fe_2$	23.6	10.0	66.4	0.71:0.30:2.00
$Y_{0.5}Zr_{0.5}Fe_2$	16.8	16.4	66.8	0.50:0.49:2.00

The structure stability of hydrides of Y–Zr–Fe alloys were conducted by the density function theory calculation under the generalized gradient approximation. By the projected augmented wave method [39,40], the exchange-correlation was simulated using the generalized gradient approximation (GGA) with Perdew-Burke-Ernzerhof (PBE) scheme [41], as implemented in the Vienna Ab-initio Simulation Package [42,43]. An energy cutoff of 500 eV for the plane-wave basis set was employed. The Monkhorst-Pack k-point meshe of 9 × 9 × 9 was used for the conventional cubic cell of the system. All the structures were fully optimized until the change in the energy between two ionic steps is smaller than 1 meV.

The computed hydrogen binding energy E_B is defined as follows:

$$E_B = \frac{1}{n}\left[\left(E_{AB_2H_n}\right) - \left(E_{AB_2}\right) - \frac{n}{2}E_{H_2}\right]$$

where $E_{AB_2H_n}$ is the total energy of AB_2 containing n H atoms, E_{AB_2} is the total energy of AB_2 without H and E_{H_2} is the hydrogen molecule energy. The energies of AB_2 with and without H atoms were calculated with the same parameters. The third part of the formula E_{H_2} was calculated by locating a H_2 molecule in a 10 Å cubic cell sides.

Results and discussions

Structure of Y–Zr–Fe alloys at different states

To demonstrate the composition and homogeneity of as-annealed $Y_{1-x}Zr_xFe_2$ (x = 0.1, 0.2, 0.3, 0.5) alloys, all ingots were characterized by back-scattering SEM (BSE) and energy-dispersive spectrometer (EDS). The BSE images (Fig. 1) show a homogeneous single phase microstructure for all the alloys, and no second phase is found. The EDS elemental mapping results demonstrate that Y, Zr and Fe elements are uniformly distributed, and the atomic percentage of Y–Zr–Fe alloys are

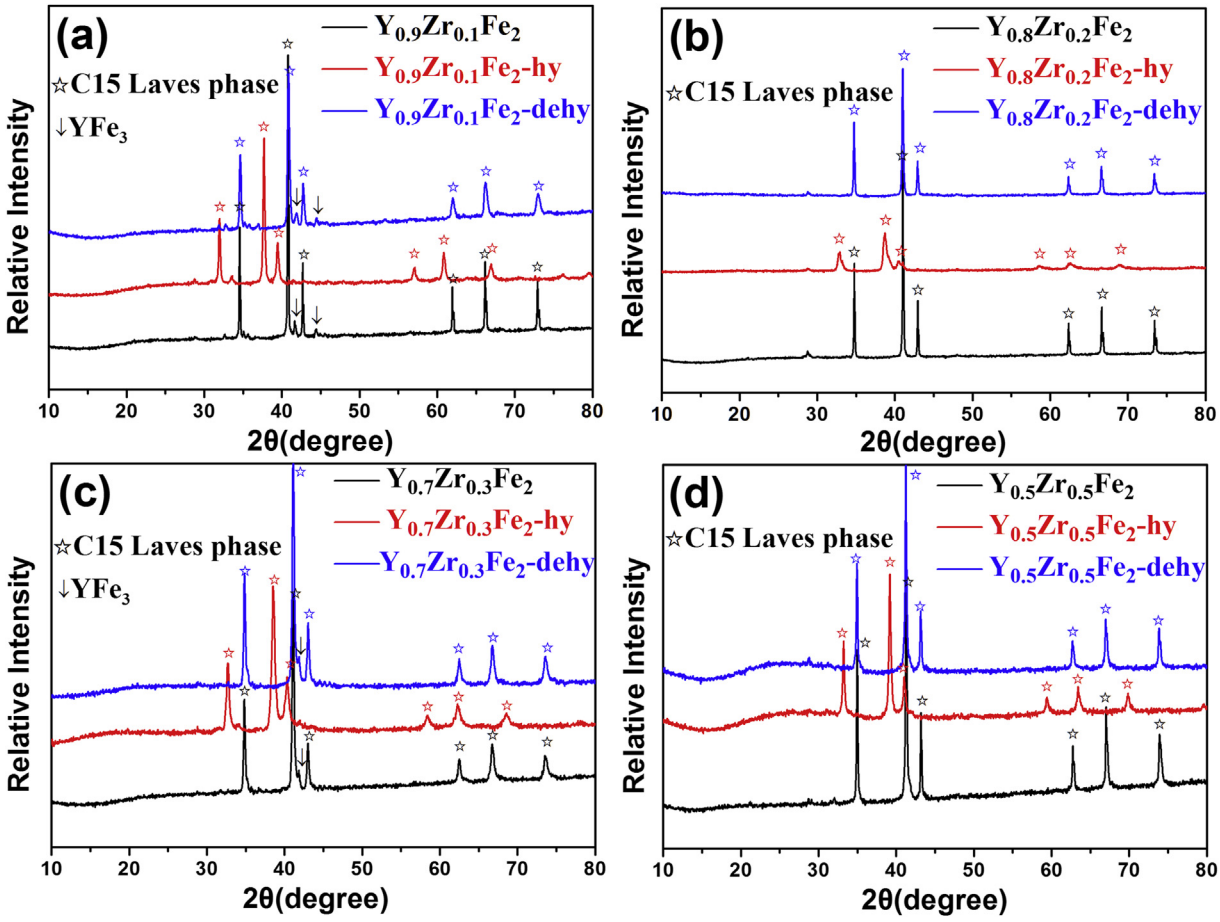

Fig. 2 – XRD patterns of $Y_{1-x}Zr_xFe_2$ ($x = 0.1, 0.2, 0.3, 0.5$) alloys at different states.

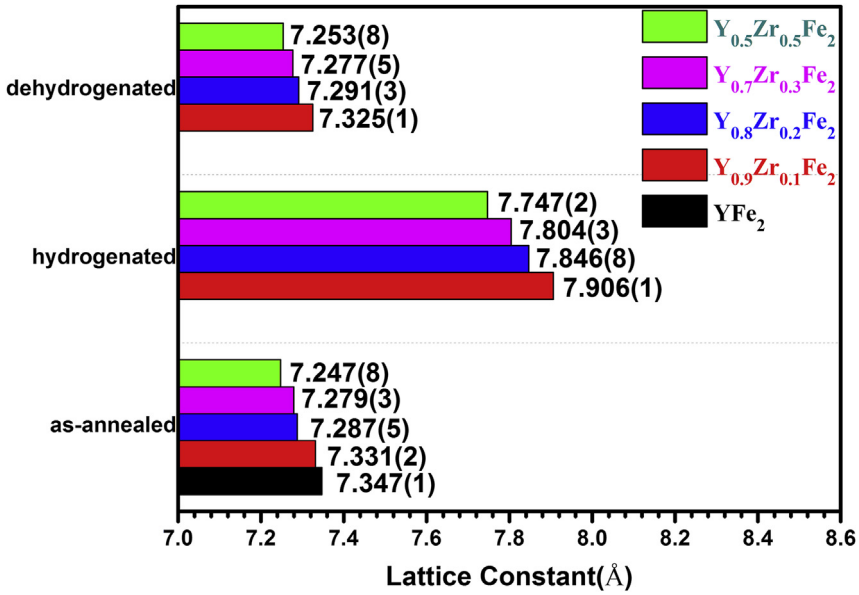

Fig. 3 – Lattice constants of Y-Zr-Fe alloys at as-annealed, hydrogenated and dehydrogenated states.

given in Table 1. The result indicates that the chemical compositions of the prepared Y–Zr–Fe alloys are consistent with the nominal compositions.

The single phase structure of alloys is further confirmed by the XRD analysis. The XRD patterns of $Y_{1-x}Zr_xFe_2$ ($x = 0.1$, 0.2, 0.3, 0.5) alloys at as-annealed state are shown in Fig. 2a–d. Fig. S1a further gives the XRD Rietveld refinement results, and the lattice constants of as-annealed Y–Zr–Fe alloys obtained from the refinements are summarized in Fig. 3. It can be seen in Fig. 2 that all as-annealed alloys have

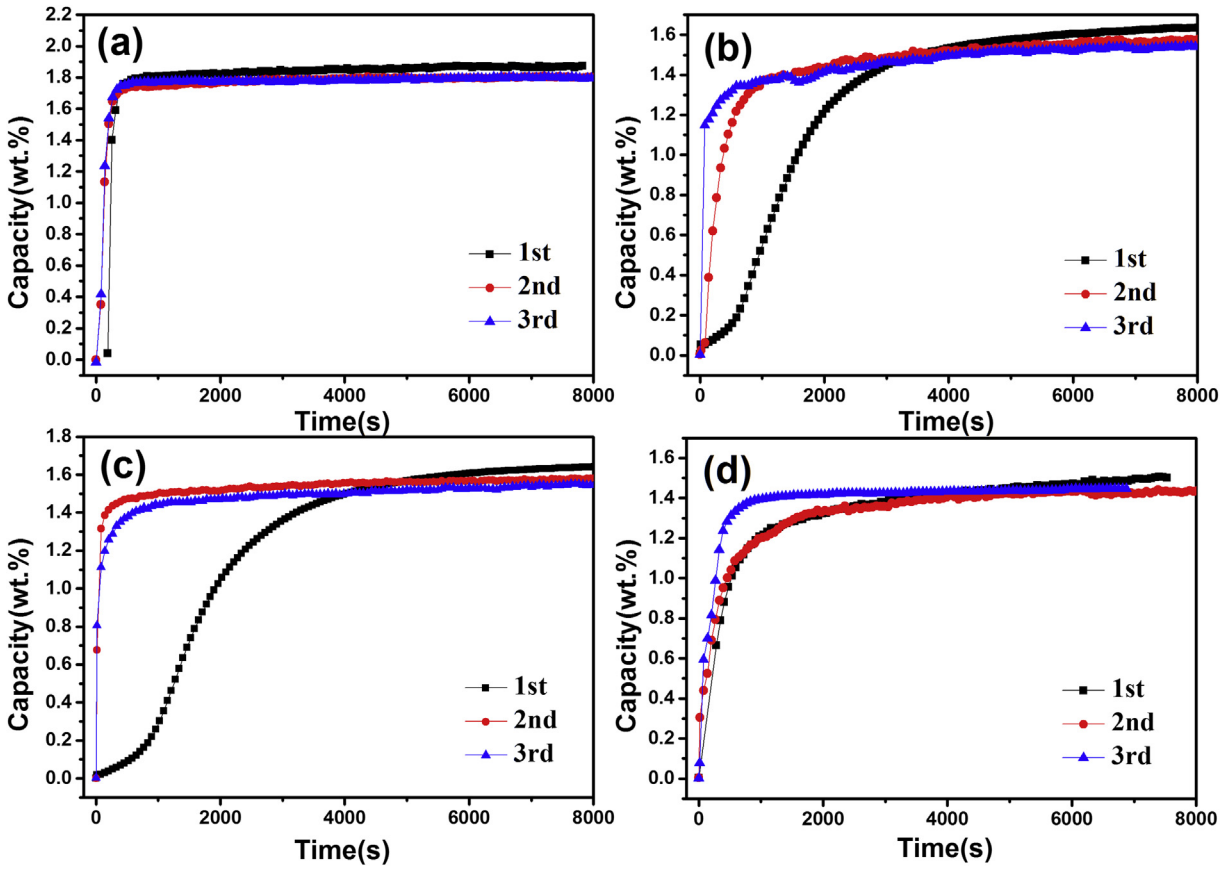

Fig. 4 – Hydrogen absorption kinetic curves of Y-Zr-Fe alloys under 4 MPa H_2 at 100 °C.

typical cubic C15 Laves phase structure ($MgCu_2$ type) with $Fd\bar{3}m$ space group. In addition, the weak additional peaks in Fig. 2a and c could be assigned to the YFe_3 phase, indicating the existence of small amount of second phase in the $Y_{0.9}Zr_{0.1}Fe_2$ and $Y_{0.7}Zr_{0.3}Fe_2$ alloys even though long time of high temperature annealing. Compared to the lattice constant of YFe_2, a reduction of lattice constant of Y–Zr–Fe alloys can be observed with the increase of Zr content as shown in Fig. 3, which is from 7.3471 Å for the YFe_2 alloy to 7.2478 Å for the $Y_{0.5}Zr_{0.5}Fe_2$ alloy. This is due to smaller atomic radius of Zr (1.59 Å) than that (1.78 Å) of Y. This result also indicates that Zr replace Y instead of Fe in the crystal lattice of YFe_2.

Fig. 2 also shows the XRD patterns of $Y_{1-x}Zr_xFe_2$ ($x = 0.1, 0.2, 0.3, 0.5$) alloys at hydrogenated and dehydrogenated states. It is clearly seen that the C15 Laves phase structure remains after the hydrogenation and dehydrogenation for each Y–Zr–Fe alloy, and no hydrogen-induced amorphization or disproportionation could be found. Conversely, Li et al. [23] ever reported that the diffraction peaks of YH_2, YH_3 and Fe appeared in the hydrogenated YFe_2 sample. Hydrogen atoms located in the matrix can be treated as point defects, and they will impose an elastic stress on the C15 phase [28] and results in its disproportionation or amorphization. Since the high bulk modulus of Zr compare with Y, Zr substitution in Y–Zr–Fe alloys could ease that elastic stress of inducing H, and thus increasing the stability of the C15 Laves phase structure, and impeding the amorphization.

As also shown in Fig. 2, the diffraction peaks of C15 Laves phase shift towards lower angle after hydrogenation, and nearly recover to the as-annealed state after dehydrogenation. This result indicates the Y–Zr–Fe alloys form reversible interstitial hydrides in the hydrogenation. Fig. S1b and Fig. S1c further give the XRD Rietveld refinement results of alloys at hydrogenated and dehydrogenated states, and the calculated lattice constants are compared with those at as-annealed state in Fig. 3. According to lattice constants in Fig. 3, the calculated percentage of cell volume increase for the alloys $Y_{1-x}Zr_xFe_2$ ($x = 0.1, 0.2, 0.3, 0.5$) are 25.42%, 24.84%, 23.24% and 22.13%, respectively. In addition, there is a very small difference in the lattice constant between dehydrogenated and as-

Table 2 – The hydrogen sorption capacity of $Y_{1-x}Zr_xFe_2$ alloys under different conditions.

Alloys	Absorption capacity/wt.%			Desorption capacity/wt.%		
	1st	2nd	3rd	100 °C	200 °C	300 °C
$Y_{0.9}Zr_{0.1}Fe_2$	1.87	1.81	1.80	0.21	0.30	0.41
$Y_{0.8}Zr_{0.2}Fe_2$	1.65	1.61	1.58	0.32	0.52	0.67
$Y_{0.7}Zr_{0.3}Fe_2$	1.60	1.58	1.57	0.51	0.74	0.88
$Y_{0.5}Zr_{0.5}Fe_2$	1.44	1.40	1.40	0.65	0.89	1.26

Table 3 – Lattice constants and electron concentration (e/a) of $Y_{1-x}Zr_xFe_2$ alloys.

As-annealed alloys	a_1/Å	Electron concentration(e/a)*
YFe_2 [47]	7.347 (1)	1.00
$Y_{0.9}Zr_{0.1}Fe_2$	7.331 (2)	1.03
$Y_{0.8}Zr_{0.2}Fe_2$	7.287 (5)	1.07
$Y_{0.7}Zr_{0.3}Fe_2$	7.279 (3)	1.10
$Y_{0.5}Zr_{0.5}Fe_2$	7.247 (8)	1.17

* e/a = $Z_1C_1+Z_2C_2+\ldots+Z_mC_m$. In the formula, Z_i (i = 1-m) is the valence electron number of group i, and C_i is the atomic percentage of group I ($C_1+C_2+\ldots+C_m=1$). For group VIII, the number of valence electrons is zero (Z = 0), and for other groups, the number of valence electrons is equal to group number in the periodic table (Z = N).

annealed states, which means few hydrogens left in the lattice.

Hydrogen storage properties of Y–Zr–Fe alloys

Fig. 4 displays the cyclic hydrogen absorption kinetic curves of $Y_{1-x}Zr_xFe_2$ (x = 0.1, 0.2, 0.3, 0.5) alloys under 4 MPa hydrogen pressure at 100 °C. It should be noted that the hydrogenated samples were dehydrogenated under dynamic vacuum at 300 °C for 2 h to ensure complete dehydrogenation. All Y–Zr–Fe alloys exhibit fast hydriding kinetics, and only the $Y_{0.8}Zr_{0.2}Fe_2$ and $Y_{0.7}Zr_{0.3}Fe_2$ alloys require ~4000 s to complete the initial hydrogen absorption. The cyclic hydrogen absorption capacities are summarized in Table 2. It is shown that all Y–Zr–Fe alloys show almost no capacity loss within three cycles, implying the reversible hydrogen storage properties of Y–Zr–Fe alloys.

As also shown in Table 2, the $Y_{0.9}Zr_{0.1}Fe_2$ alloy delivers the highest initial hydrogen absorption capacity of 1.87 wt.% H. Comparatively, the $Y_{0.8}Zr_{0.2}Fe_2$, $Y_{0.7}Zr_{0.3}Fe_2$ and $Y_{0.5}Zr_{0.5}Fe_2$ alloys can absorb 1.65 wt.%, 1.60 wt.% and 1.44 wt.% H in the 1st cycle, respectively. This notable reduction of hydrogen absorption capacity with the increasing of Zr content should be related to the structural change in the lattice constants and electron concentration (e/a) by the Zr substitution. Table 3 compares the electron concentration and lattice constant of Y–Zr–Fe alloys. The Y substitution by Zr in the YFe_2 alloy results in the decreases in the lattice constant but the increases in the electron concentration. According to Wagner 's [44] theory, the higher electron concentration would result in the lower hydrogen absorption capacity, because more outer electrons of the alloy would exert stronger repulsive interaction to the hydrogen atoms, and thus hindering the hydrogen atoms into the lattice. Regarding to the effect of lattice constant, only A_2B_2 sites are found occupied in $YFe_2D_{3.5}$ [45], but for larger D content (4.2 D/f.u.), a few part of D atoms are located in AB_3 sites (3 among 18 sites for x = 4.2 in YFe_2D_x) [46]. Therefore, the increasing Zr content leads to smaller size of A_2B_2 and AB_3 sites of Y–Zr–Fe alloys, which means the larger volume expansion and stress of crystal lattice induced by the

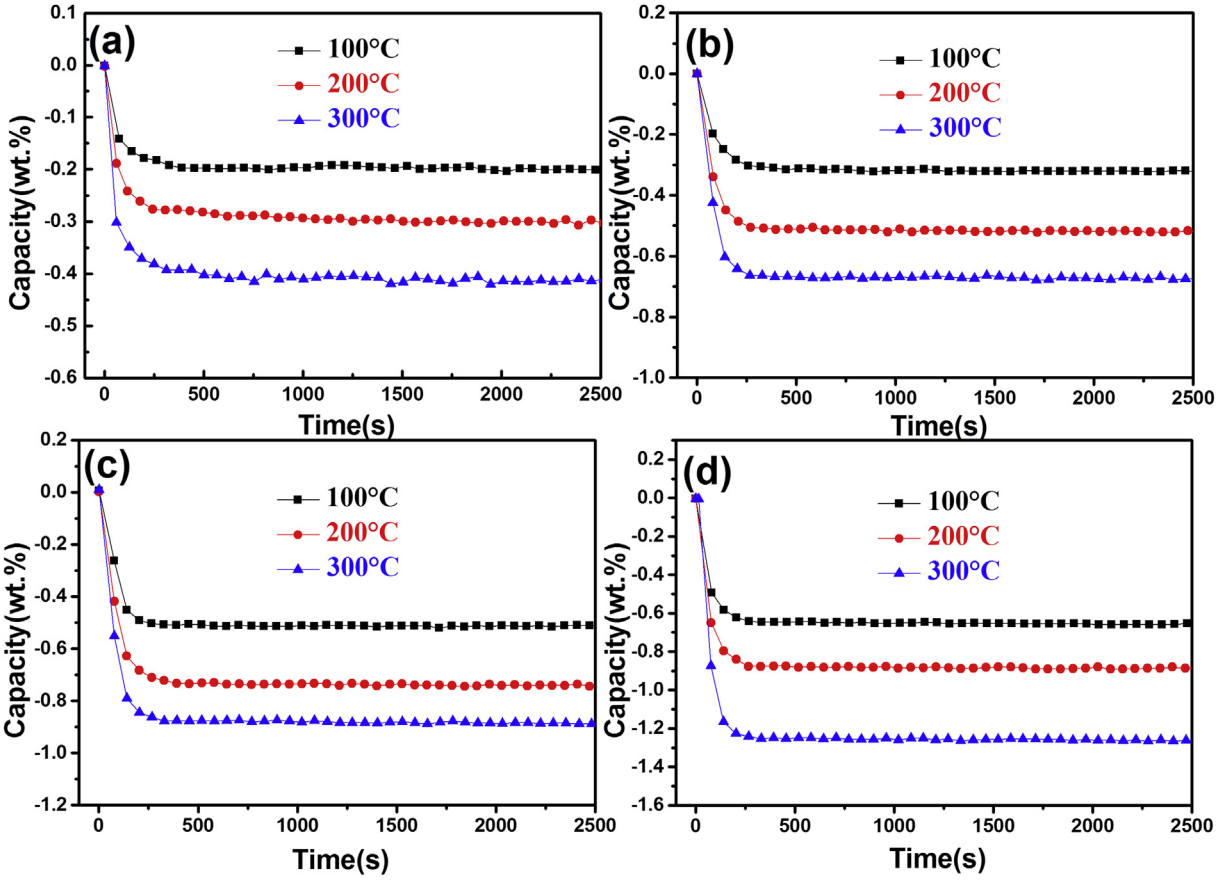

Fig. 5 – Hydrogen desorption kinetic curves of Y-Zr-Fe alloys under static vacuum at different temperatures.

hydrogenation. This would make it more difficult for the part of A_2B_2 or AB_3 tetrahedral sites to be occupied by hydrogen atoms. As a result, the hydrogen absorption capacity decreases with the increasing of Zr content.

Hydrogen desorption kinetic curves of $Y_{1-x}Zr_xFe_2$ ($x = 0.1$, 0.2, 0.3, 0.5) alloys under static vacuum at different temperatures are presented in Fig. 5, and the obtained desorption capacities are also listed in Table 2. All Y–Zr–Fe alloys show fast dehydrogenation rate, and the saturation dehydrogenation capacity could be reached within 500 s. It is seen that more hydrogen is released with the increasing desorption temperature. It also shows that the Y–Zr–Fe alloy with higher Zr content releases more hydrogen at the same temperature, a maximum dehydrogenation capacity of 1.26 wt.% is obtained for the alloy $Y_{0.5}Zr_{0.5}Fe$ at 300 °C. However, the hydrogen desorption capacities of all Y–Zr–Fe alloys are lower than their hydrogenation capacities. The rehydrogenation results, as shown in Fig. 4, indicates that the residual hydrogen in the Y–Zr–Fe alloys could be fully released under the condition of dynamic vacuum, these results imply that the incomplete dehydrogenation of Y–Zr–Fe alloys is due to the relatively low dehydriding equilibrium pressure. Similar situation was also found in the Y–Fe–Al alloys, which showed reversible hydrogen storage properties due to the partial Al substitution at the B-site [23]. However, the Y–Fe–Al alloys shows rather low dehydrogenation capacity (<0.56 wt.% H) under static vacuum condition, and the dehydrogenation capacity rarely increase with the increasing Al content. Therefore, the increased dehydrogenation capacity of Y–Zr–Fe alloys with the Zr content implies the improvement of dehydriding equilibrium pressure.

Fig. 6 shows the desorption PCI curves of $Y_{1-x}Zr_xFe_2$ ($x = 0.1$, 0.2, 0.3, 0.5) alloys at 200 °C. The hydrogen desorption capacities of the Y–Zr–Fe alloys at 200 °C are much close to those obtained by isothermal kinetic test. Similar to previously reported Y–Fe–Al alloys and ZrV_2-based alloys [48], only sloping PCI curves are observed for the alloys $Y_{0.9}Zr_{0.1}Fe_2$ and $Y_{0.8}Zr_{0.2}Fe_2$. Comparatively, there exist similar PCI curves with larger sloping at the high-pressure region for the alloys $Y_{0.7}Zr_{0.3}Fe_2$ and $Y_{0.5}Zr_{0.5}Fe_2$. The PCI results could well explain the incomplete dehydrogenation as shown in Fig. 5. The

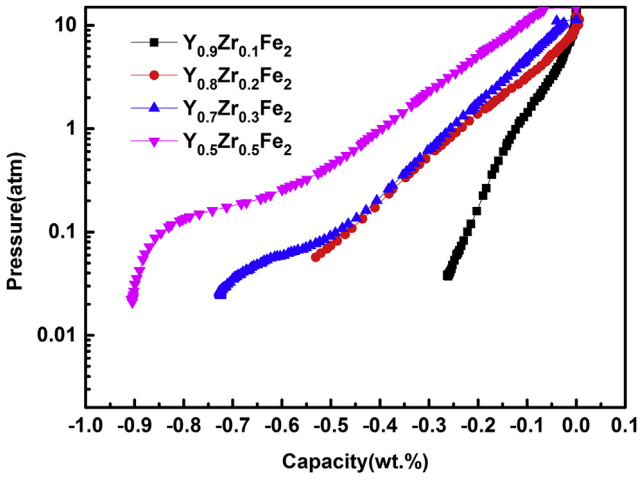

Fig. 6 – PCI desorption curves of Y-Zr-Fe alloys at 200 °C.

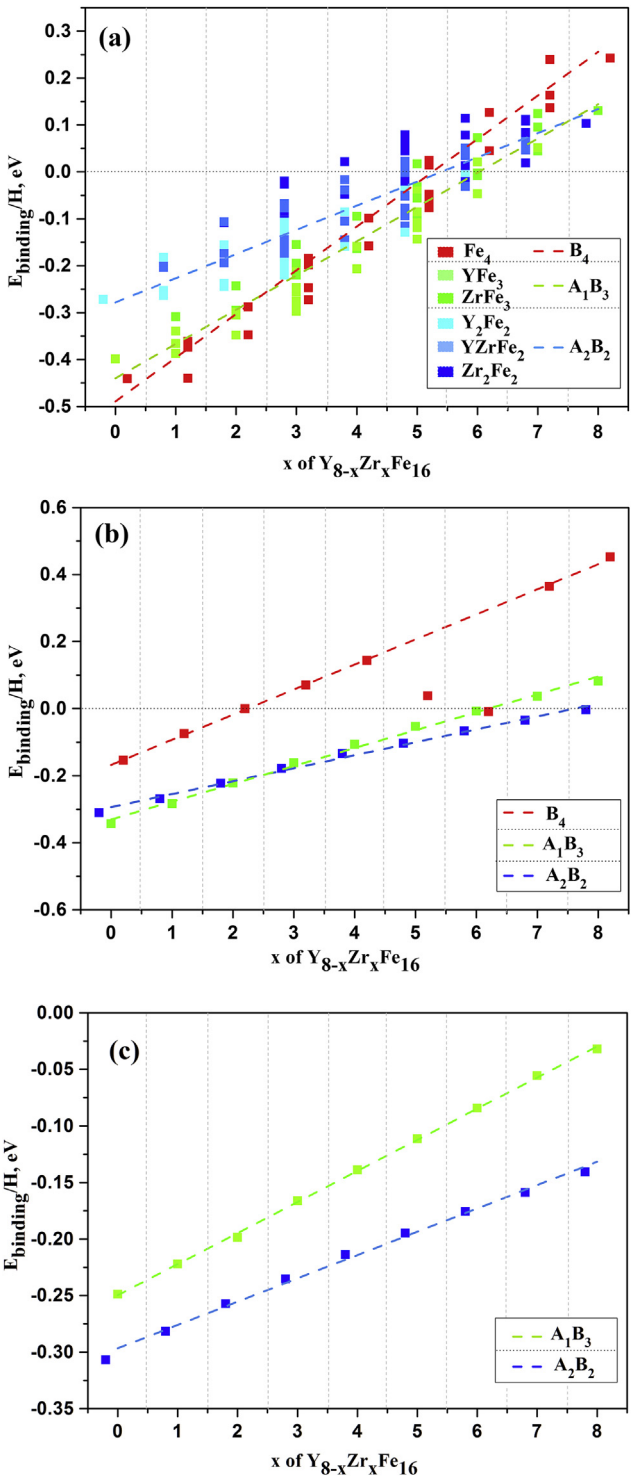

Fig. 7 – Binding energy of hydrogen atoms in A_2B_2, A_1B_3 or B_4 tetrahedral interstitial sites of $Y_{8-x}Zr_xFe_{16}$, (a) $Y_{8-x}Zr_xFe_{16}H_1$, (b) $Y_{8-x}Zr_xFe_{16}H_8$, (c) $Y_{8-x}Zr_xFe_{16}H_{32}$.

dehydriding equilibrium pressure of the alloys is decreased with the increasing hydrogen release content, and the dehydrogenation process would be terminated as the hydrogen pressure in the sample chamber is higher than the equilibrium pressure of the alloys.

With the increasing Zr content, the Y–Zr–Fe alloys exhibits a short dehydriding plateau at the low-pressure region for the alloys $Y_{0.7}Zr_{0.3}Fe_2$ and $Y_{0.5}Zr_{0.5}Fe_2$. Furthermore, the plateau pressure for the alloy $Y_{0.5}Zr_{0.5}Fe_2$ is higher than that for the alloy $Y_{0.7}Zr_{0.3}Fe_2$. This phenomenon could not be observed in our previous work on the Y–Fe–Al system with reversible hydrogen storage properties. This result also explains that the $Y_{0.5}Zr_{0.5}Fe_2$ alloy has higher dehydrogenation capacity than other Y–Zr–Fe alloys. Therefore, the Zr substitution greatly improves the dehydriding thermodynamics of YFe_2.

The improved dehydriding thermodynamic properties of Y–Zr–Fe alloys should be related to the decreased lattice constant by the substitution of Y with Zr, and smaller tetrahedral interstitial size leads to the increase of equilibrium pressure of dehydriding reaction. In addition, according to Bereznitsky and Jacob et al.'s theory [49,50], the elevation of dehydriding equilibrium pressure is indicative of the increasing hydrogen-hydrogen attractive interaction and decreasing metal-hydrogen attractive interaction, namely that the hydride of Y–Zr–Fe alloys becomes unstable. To further reveal the correlation of hydride stability with the Zr content, the formation energies of Y–Zr–Fe–H hydrides with different H and Zr contents were calculated by first-principle local-density-function theory.

Fig. 7 shows the calculated binding energies of hydrogen atoms in A_2B_2, A_1B_3 or B_4 tetrahedral interstitial sites of $Y_{8-x}Zr_xFe_{16}$ hydrides. Considering there is not enough number of B_4 tetrahedral sites per unite cell to provide the occupation of 32 hydrogen atoms, thus only the binding energies in A_2B_2 and A_1B_3 tetrahedral were calculated for the hydride $Y_{8-x}Zr_xFe_{16}H_{32}$ (Fig. 7c). As shown in Fig. 7a, the binding energies in A_2B_2, A_1B_3 or B_4 tetrahedral interstitial sites increase with increasing x value in the $Y_{8-x}Zr_xFe_{16}H_1$ hydride, indicating that this hydride becomes unstable with increasing Zr content. When adding more hydrogen atoms into the unit cell and forming the hydrides $Y_{8-x}Zr_xFe_{16}H_8$ (Fig. 7b) and $Y_{8-x}Zr_xFe_{16}H_{32}$ (Fig. 7c), the binding energies in A_2B_2, and A_1B_3 tetrahedral sites still increase with increasing Zr content. As shown in Fig. 7b, there are two abnormal points for the hydrogen occupation in the small B_4 tetrahedral site because of structural distortion. These results clear demonstrate that the Zr substitution in YFe_2 alloy decreases the thermodynamic stability of hydrides.

Conclusions

We have successfully eliminated the hydrogenation-induced amorphization and disproportionation of YFe_2 by partial substitution of Y with Zr. All $Y_{1-x}Zr_xFe_2$ ($x = 0.1, 0.2, 0.3, 0.5$) alloys remained C15 Laves phase structure during de-/hydrogenation cycles, and reversible hydrogen storage properties were achieved. With the increasing Zr content, the Y–Zr–Fe alloys showed a decrease in the lattice constant and hydrogen absorption capacity, but an increase in the hydrogen desorption capacity and dehydriding equilibrium pressure. The alloy $Y_{0.5}Zr_{0.5}Fe_2$ delivered the highest hydrogen desorption capacity and a distinct dehydriding plateau appeared in the PCI curve. The experimental and computational results clearly indicated that the dehydriding thermodynamic properties of YFe_2 alloy could be greatly improved by the alloying with Zr. Our work shows the potential of Y–Zr–Fe ternary alloys for reversible hydrogen storage.

Acknowledgements

We acknowledge financial support from the National Natural Science Foundation of China (Grant Nos. U1601212, 51571091 and 51671089), the Fund for Innovative Research Groups of the National Natural Science Foundation of China (Grant No. 51621001), and Natural Science Foundation of Guangdong Province (2016A030312011).

Appendix A. Supplementary data

Supplementary data related to this article can be found at https://doi.org/10.1016/j.ijhydene.2018.05.161.

REFERENCES

[1] Bélafi-Bakó K, Búcsú D, Pientka Z, Bálint B, Herbel Z, Kovács KL, et al. Integration of biohydrogen fermentation and gas separation processes to recover and enrich hydrogen. Int J Hydrogen Energy 2006;31:1490–5.
[2] Majlan EH, Wan RWD, Iyuke SE, Mohamad AB, Kadhum AAH, Mohammad AW, et al. Hydrogen purification using compact pressure swing adsorption system for fuel cell. Int J Hydrogen Energy 2009;34:2771–7.
[3] Buttner WJ, Post MB, Burgess R, Rivkin C. An overview of hydrogen safety sensors and requirements. Int J Hydrogen Energy 2011;36:2462–70.
[4] Sakintuna B, Lamari-Darkrim F, Hirscher M. Metal hydride materials for solid hydrogen storage: a review. Int J Hydrogen Energy 2007;32:1121–40.
[5] Dornheim M. Thermodynamics of metal hydrides: tailoring reaction enthalpies of hydrogen storage materials. In: Moreno JC, editor. Thermodynamics-interaction studies-solids, liquids, gases. Germany: InTech; 2011. p. 891–914.
[6] Kodama T. Proposal for new indexes describing the degree of hysteresis and those applications to the $ZrMn_2H_2$ systems. J Alloy Comp 1998;278:194–200.
[7] Kodama T, Anada H, Kaminaka H. The site occupancies for the excess manganese atoms and the third element niobium in the intermetallic compound $ZrMn_2$. J Alloy Comp 1995;224:1485–94.
[8] Joubert JM, Latroche M, Percheron-Guégan A. Hydrogen absorption properties of several intermetallic compounds of the Zr-Ni system. J Alloy Comp 1995;231:494–7.
[9] Cao Z, Ouyang L, Hui W, Liu J, Sun D, Zhang Q, et al. Advanced high-pressure metal hydride fabricated via Ti–Cr–Mn alloys for hybrid tank. Int J Hydrogen Energy 2015;40:2717–28.
[10] Sivov RB, Zotov TA, Verbetsky VN. Hydrogen sorption properties of $ZrFe_x$ ($1.9 \leq x \leq 2.5$) alloys. Int J Hydrogen Energy 2011;36:1355–8.
[11] Zotov T, Movlaev E, Mitrokhin S, Verbetsky V. Interaction in $(Ti,Sc)Fe_2$–H_2 and $(Zr,Sc)Fe_2$–H_2 systems. J Alloy Comp 2008;459:220–4.
[12] Cao Z, Ouyang L, Wang H, Liu J, Sun L, Felderhoff M, et al. Development of Zr–Fe–V alloys for hybrid hydrogen storage system. Int J Hydrogen Energy 2016;41:11242–53.

[13] Aoki K, Yamamoto T, Masumoto T. Hydrogen induced amorphization in RNi_2 laves phases. Scripta Metall Mater 1987;21:27–31.

[14] Aoki K, Yamamoto T, Satoh Y, Fukamichi K, Masumoto T. Amorphization of the $CeFe_2$ Laves phase compound by hydrogen absorption. Acta Metall 1987;35:2465–70.

[15] Dilixiati M, Kanda K, Ishikawa K, Aoki K. Hydrogen-induced amorphization in C15 Laves phases RFe_2. J Alloy Comp 2002;337:128–35.

[16] Aoki K, Li HW, Ishikawa K. Process and mechanism of hydrogen-induced amorphization in C15 Laves phases RFe_2. J Alloy Comp 2005;404–406:559–64.

[17] Dilixiati M, Kanda K, Ishikawa K, Aoki K. Hydrogen absorbing materials. Pressure dependence of hydrogen-induced amorphization in C15 laves phase $TbFe_2$. Mater Trans 2002;43:1089–94.

[18] Aoki K, Masumoto T. Hydrogen-induced amorphization of intermetallics. J Alloy Comp 1995;231:20–8.

[19] Aoki K. Amorphous phase formation by hydrogen absorption. Mater Sci Eng A 2001;304–306:45–53.

[20] Luo S, Clewley JD, Flanagan TB. The thermodynamic characterization of the H-induced amorphization of $CeFe_2$ and the determination of the energy site distribution using reaction calorimetry. Acta Mater 1996;44:4187–93.

[21] Meng WJ, Okamoto PR, Thompson LJ, Kestel BJ, Rehn LE. Hydrogen–induced crystal to glass transformation in Zr_3Al. Appl Phys Lett 1988;53:1820–2.

[22] Leblond T, Paul-Boncour V, Cuevas F, Isnard O, Fernández JF. Study of the multipeak deuterium thermodesorption in YFe 2 D x ($1.3 \leq x \leq 4.2$) by DSC, TD and in situ neutron diffraction. Int J Hydrogen Energy 2009;34:2278–87.

[23] Li Z, Wang H, Ouyang L, Liu J, Zhu M. Reversible hydriding in $YFe_{2-x}Al_x$ (x=0.3, 0.5, 0.7) intermetallic compounds. J Alloy Comp 2016;689:843–8.

[24] Aoki K, Li HW, Dilixiati M, Ishikawa K. Formation of crystalline and amorphous hydrides by hydrogenation of C15 Laves phase YFe_2. Mater Sci Eng A. 2007;449:2–6.

[25] Chung U, Kim Y, Lee J. General features of hydrogen-induced amorphization in RM(R = rare earth, M = transition element) Laves phases. Phil Mag B 1991;63:1119–30.

[26] Rice RC, Bowman RS. Effect of sample size on parameter estimates in solute-transport experiments. Soil Sci 1988;146:108–12.

[27] Krebs HU, Samwer K. Crystal-glass transition in Zr-Co multilayers observed by in situ X-ray diffraction measurements. Europhys Lett 1986;2:141–8.

[28] Kim YG, Lee JY. The mechanism of hydrogen-induced amorphization in intermetallic compounds. J Alloy Comp 1992;187:1–7.

[29] Pearson GL. Mechanical properties of intermetallic compounds. J Am Chem Soc 1960;82:5258.

[30] Kojima Y, Kawai Y, Towata SI, Matsunaga T, Shinozawa T, Kimbara M. Development of metal hydride with high dissociation pressure. J Alloy Comp 2006;419:256–61.

[31] Ramesh R, Annapoorni S, Rao KVSR. Solubility of hydrogen in $Zr_{1-x}Ho_xCo_2$ ($0 \leq x \leq 1$) alloys. J Less Common Met 1991;170:75–82.

[32] Ramesh R, Rao KVSR. Hydrogen absorption characteristics of the $Zr_{1-x}Ho_xCo_2$ system in the pressure range 0–40 bar. J Alloy Comp 1993;191:101–5.

[33] Kesavan TR, Ramesh R, Rao KVSR. Hydrogen absorption studies in $Zr_{0.4}Ho_{0.6}Fe_2$. J Alloy Comp 1995;226:46–50.

[34] Kesavan TR, Ramaprabhu S, Rao KVSR, Das TP. Hydrogen absorption and kinetic studies in $Zr_{0.2}Ho_{0.8}Fe_2$. J Alloy Comp 1996;244:164–9.

[35] Paul-Boncour V, Bourée F, Filipek SM, Marchuck I, Jacob I, Percheronguegan A. Neutron diffraction study of ZrM_2D_x deuterides (M=Fe, Co). J Alloy Comp 2003:356–7.

[36] Merlino AR, Luna CR, Juan A, Pronsato ME. A DFT study of hydrogen storage in $Zr(Cr_{0.5}Ni_{0.5})_2$ Laves phase. Int J Hydrogen Energy 2016;41:2700–10.

[37] Gesari SB, Pronsato ME, Visintin A, Juan A. Hydrogen storage in AB_2 laves phase (A=Zr, Ti; B=Ni, Mn, Cr, V): binding energy and electronic structure. J Phys Chem C 2010;114:16832–42.

[38] Lindbaum A, Hafner J, Gratz E, Heathman S. Structural stability of YM_2 compounds (M=Al, Ni, Cu) studied by ab initio total-energy calculations and high-pressure x-ray diffraction. J Phys Condens Matter 1998;10:2933.

[39] Kresse G. From ultrasoft pseudopotentials to the projector augmented-wave method. Phys Rev B Condens Matter 1999;59:1758–75.

[40] PE B. Projector augmented-wave method. Phys Rev B Condens Matter 1994;50:17953–79.

[41] Zhang Y, Yang W. Comment on "generalized gradient approximation made simple". Phys Rev Lett 1997;890.

[42] Kresse G, Furthmüller J. Efficiency of ab-initio total energy calculations for metals and semiconductors using a plane-wave basis set. Comput Mater Sci 1996;6:15–50.

[43] Kresse G, Furthmüller J. Efficient iterative schemes for ab initio total-energy calculations using a plane-wave basis set. Phys Rev B Condens Matter 1996;54:11169.

[44] Wagner C. Thermodynamics of alloys. In: Mellgren S, editor. Metallurgy and materials. Cambridge: Addision-Wesley Press; 1983. p. 136–7.

[45] Latroche M, Paul-Boncour V, Percheron-Guégan A, Bourée-Vigneron F. Crystallographic study of $YFe_2D_{3.5}$ by x-ray and neutron powder diffraction. J Solid State Chem 1997;133:568–71.

[46] Ropka J, Černý R, Paul-Boncour V, Proffen T. Deuterium ordering in Laves-phase deuteride $YFe_2D_{4.2}$. J Solid State Chem 2009;182:1907–12.

[47] Mal HHV, Buschow KHJ, Miedema AR. Hydrogen absorption of rare-earth (3 d) transition intermetallic compounds. J Less Common Met 1976;49:473–5.

[48] Dan L, Biriş AR, Indrea E, Biriş AS, Bele G, Schlapbach L, et al. Hydrogen absorption and hydride electrode behaviour of the Laves phase $ZrV_{1.5-x}Cr_xNi_{1.5}$. J Alloy Comp 1999;291:289–94.

[49] Bereznitsky M, Jacob I, Bloch J, Mintz MH. Thermodynamic and structural aspects of hydrogen absorption in the $Zr(Al_xFe_{1-x})_2$ system. J Alloy Comp 2002;351:180–3.

[50] Jacob I, Bereznitsky M. Experimental elucidation of the anomalous hydrogen absorption in Al-containing pseudobinary intermetallic compounds. J Alloy Comp 2002;336:L1–3.